

Single-atom Pd-Ru pair on Pt surface for promoting hydrogen oxidation in alkaline media

Longsheng Cao

Material Science and Engineering Department, UMD <https://orcid.org/0000-0002-2917-6523>

Fernando Soto

Texas A&M University

Dan Li

University of Maryland, College Park

Tao Deng

University of Maryland, College Park

Enyuan Hu

Chemistry Division, Brookhaven National Laboratory <https://orcid.org/0000-0002-1881-4534>

Nico Eidson

University of Maryland, College Park

Xiao-Qing Yang

Brookhaven National Laboratory <https://orcid.org/0000-0002-3625-3478>

Perla B Balbuena

Texas A&M University <https://orcid.org/0000-0002-2358-3910>

Chunsheng Wang (✉ cswang@umd.edu)

University of Maryland, College Park <https://orcid.org/0000-0002-8626-6381>

Article

Keywords: hydrogen oxidation reaction, HOR, Pt nanocatalysts, single-atom Pd-Ru pair

Posted Date: August 4th, 2020

DOI: <https://doi.org/10.21203/rs.3.rs-48639/v1>

License:  This work is licensed under a Creative Commons Attribution 4.0 International License.

[Read Full License](#)

Single-atom Pd-Ru pair on Pt surface for promoting hydrogen oxidation in alkaline media

Longsheng Cao^{1†}, Fernando A. Soto^{2†}, Dan Li¹, Tao Deng¹, Enyuan Hu³, Nico Eidson¹, Xiao-Qing Yang³, Perla B. Balbuena^{2,4*}, and Chunsheng Wang^{1,5*}

¹ Department of Chemical and Biomolecular Engineering, University of Maryland, College Park, MD 20742, USA

² Department of Chemical Engineering, Texas A&M University, College Station, Texas 77843, USA

³ Chemistry Division, Brookhaven National Laboratory, Upton, NY 11973, USA

⁴ Department of Materials Science and Engineering, Texas A&M University, College Station, Texas 77843, USA

⁵ Department of Chemistry and Biochemistry, University of Maryland, College Park, MD 20742, USA

† These authors contributed equally: Longsheng Cao, Fernando A. Soto.

*e-mail: cswang@umd.edu; balbuena@tamu.edu

Abstract: The hydrogen oxidation reaction (HOR) in alkaline media is critical for the alkaline fuel cell and electrochemical ammonia compressor. The sluggishness of HOR in the alkaline electrolyte requires platinum nano-catalysts, which are scarce and expensive. Decorating Pt catalysts with transition metals can boost the area specific activity (SA) of Pt nano-catalysts, but it often reduces the electrochemical active surface area (ECSA), resulting in a limited enhancement in Pt mass activity (MA). Single-atom surface modification of Pt catalysts can significantly enhance the reaction kinetics of single molecule, but it is less effective for HOR process that involve multiple molecules, i.e. H₂ and OH⁻. Here we use a single-atom Pd-Ru pair to boost the activity of Pt nano-catalysts without loss of surface-active sites. Using a mildly catalytic thermal pyrolysis approach, single-Pd and single-Ru atom pair are precisely decorated on Pt nanoparticle surfaces, which is confirmed by Extended X-Ray Absorption Fine Structure (EXAFS) analysis. Density functional theory (DFT) calculations and *ab-initio* molecular dynamics (AIMD) simulations show the preferred adsorption of single-atom Pd and Ru dopants over Pd and Ru clustering on Pt surfaces. The single-atom Pd-Ru pair decorated Pt (Pd-Ru@Pt) catalyst features tri-active sites including: hydrophilic Pd promoting activation of adsorbed hydrogen atoms (H_{ads}) via the hydrogen spill-over effect, oxyphilic Ru facilitating the adsorption of hydroxide molecules (OH_{ads}), and highly-catalytic Pt facilitating water formation with increased availability of H_{ads} and OH_{ads}. In addition, the dopant decoration also reduces the hydrogen binding energy due to the shift of the (*d*) band center relative to the Fermi Level. The tri-active Pd-Ru@Pt catalyst shows 15.9 times higher area specific activity (SA) and 17.5 times larger mass activity (MA) than the state-of-the-art nano-Pt catalyst for HOR, and 2 times higher MA than nano-Pt for the hydrogen evolution reaction (HER). The mass exchange current density of single-atom Pd-Ru@Pt/C for the HOR/HER was 6.0 times that of the Pt/C, corresponding to 9.7 times that of Pd@Pt/C and 6.5 times that of Ru@Pt/C. The

superior HOR/HER performance of the tri-active site catalyst is also demonstrated in ammonia and hydrogen pumps for practical application.

Introduction

The sluggish kinetics of electrochemical hydrogen and oxygen redox reactions in alkaline electrolytes hinder the wide application of renewable energy conversion and storage devices¹ that use alkaline fuel cells^{2,3} and electrochemical gas compressors⁴. State-of-the-art electrocatalysts for these electrochemical conversion systems are usually platinum group metal (PGM)-based nanoparticles. However, the high cost of the Pt-based electrocatalysts severely limits their widespread adoption. An effective method for reducing the cost is to substantially reduce the amount of Pt required by enhancing the catalytic activity per given mass of Pt; i.e. Pt mass activity (MA).

The MA depends on both the electrochemically active surface area (ECSA) and the specific activity (SA, normalized by surface area). The ECSA can be enhanced by tailoring the geometrical structure, including ultra-small nanostructure⁵ and core-shell nanostructure with Pt skin⁶. The SA can be increased by modifying or decorating the Pt nanoparticle surface. Surface modification or decoration of Pt catalysts has been used for boosting the hydrogen evolution reaction (HER)^{7,8} and the oxygen reduction reaction (ORR)^{9,10}. For instance, decorating the Pt nanostructure surface using Ni(OH)₂ clusters⁸ greatly boosts the SA for the HER in alkaline electrolytes. However, such modification also reduces the ECSA by 30–50%⁸. For surface modification, it is extremely challenging to increase the SA without substantially sacrificing the ECSA, which is necessary for achieving a high MA in both half-cells and full-cells. It is also more challenging enhancing the hydrogen oxidation reaction (HOR) compared to the HER in alkaline electrolytes, and the HOR enhancement by surface modification of Pt-based catalysts has rarely been reported before.

To boost the HOR ($\text{H}_2 + 2\text{OH}^- \rightarrow 2\text{H}_2\text{O} + 2\text{e}^-$) on Pt, adsorption and activation of a large amount of OH_{ads} and H_{ads} surrounding Pt atoms are critical, which can be realized by decorating with Ru and Pd on the Pt surface, respectively. On Ru- and Pd-decorated Pt nanoparticles, the Ru and Pd act as catalyst promoters to increase the availability of OH_{ads} and H_{ads} surrounding Pt atoms, respectively. (**Fig. 1** and **Supplementary Fig. 1**) It is critical to reduce the decorating species' sizes to prevent surface Pt active sites from being blocked while producing as many activated Pt sites with adjacent Ru and Pd atoms as possible for improved SA for the HOR. The ultimate choice to achieve the highest MA is the use of single-atoms to decorate Pt, which allows the smallest number of Ru and Pd species to activate the most Pt atoms while minimizing blocking of surface Pt sites. However, the decorating of single Ru and single Pd atoms on the Pt surface has not been realized to date due to the limitation of current synthetic approaches.

Here, we create paired single-atom Pd-Ru doped Pt nanoparticles (single-atom Pd-Ru@Pt) with a high MA (both a high SA and a large ECSA) and a long durability. Importantly, the single-atom Pd-Ru@Pt substantially increases SA to 9.98 mA cm⁻² and MA to 4.93 A mg⁻¹_{metal} for the HOR at

–50 mV vs. reversible hydrogen electrode (RHE) at pH 13, which are 15.9 and 17.5 times higher than those of the state-of-the-art Pt/C, respectively. To the best of our knowledge, such a high MA for the HOR in alkaline solution has not been achieved by any other nanomaterials under comparable conditions. The single-atom Pd-Ru@Pt catalyst also promotes the HER. The tri-active reaction mechanism for single-atom Pd and Ru decorated Pt is validated by extended X-ray absorption fine structure (EXAFS) characterization, density functional theory (DFT) calculations, and *ab-initio* molecular dynamics (AIMD) simulations.

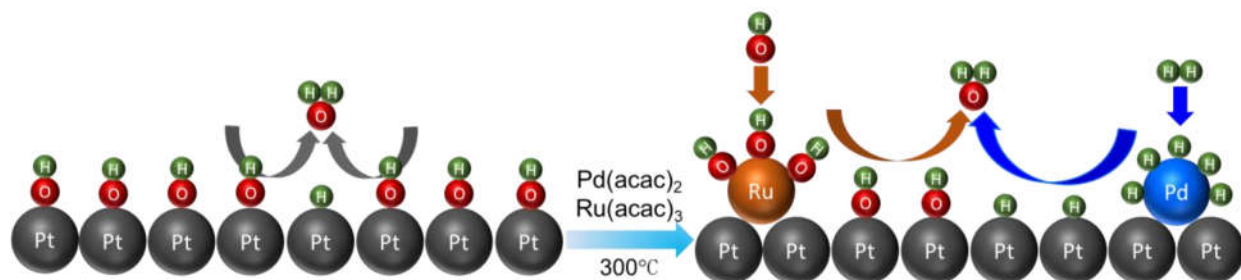


Fig. 1| Hydrogen oxidation reaction schematic diagram on Pt and single-atom Pd-Ru@Pt surface. The decoration of Pt nanoparticles with paired single-atom Pd-Ru species increases the availability of H_{ads} and OH_{ads} on the Pt surface to boost the specific catalytic activity for the HOR without sacrificing the ECSA.

Results and discussion

Synthesis and geometric structure

Inspired by the recent finding that nitrogen-rich carbon defect trapping Cu(NH₃)_x¹¹ can be used to prepare a single Cu atom catalyst, we used a vacuum assisted solid-phase synthetic approach to decorate single-atom Pd-Ru on Pt nanoparticle surfaces. As shown in **Fig. 2a**, we put carbon supported Pt nanoparticles (Pt/C) on a silicon wafer, loaded Ru(acac)₃ and Pd(acac)₂ in a combustion boat, and transferred them into a vacuumed glass tube. The Ru(acac)₃ and Pd(acac)₂ were chosen as Pd and Ru precursors because of their low evaporation temperatures. The glass tube was heated to 300°C for 3.0h. The vaporized Pd and Ru precursors were trapped by the surface defects of the Pt nanoparticles at high temperatures, generating the isolated Pd and Ru single atoms on the Pt surface via a catalytic pyrolysis effect of Pt forming single-atom Pd-Ru@Pt/C. As reference catalysts, atomic Pd doped Pt/C (Pd@Pt/C) and atomic Ru doped Pt/C (Ru@Pt/C) were also synthesized using the same method.

X-ray power diffraction (XRD) of single-atom Pd-Ru decorated Pt showed only Pt peaks (**Fig. 2b**), indicating that decorated Pd and Ru atoms did not accumulate into Pd, Ru, or alloy phases. The morphology of single-atom Pd-Ru@Pt was characterized using transmission electron microscopy (TEM). As shown in **Supplementary Fig. 2**, the single-atom Pd-Ru@Pt catalysts with an average particle size of 2.9±0.4 nm dispersed uniformly on carbon support. Comparing the average particle size of Pd-Ru@Pt with that of the original Pt nanoparticle (2.6±0.3 nm) (**Supplementary Fig. 3**), the surface decoration thickness was ~0.3 nm, corresponding to a particle

coating of one atomic layer. For the reference catalysts, the Pd@Pt/C (**Supplementary Fig. 4**) and Ru@Pt/C (**Supplementary Fig. 5**) showed good dispersion and crystal structure, with average particle sizes of 3.2 ± 0.5 and 3.7 ± 0.6 , respectively.

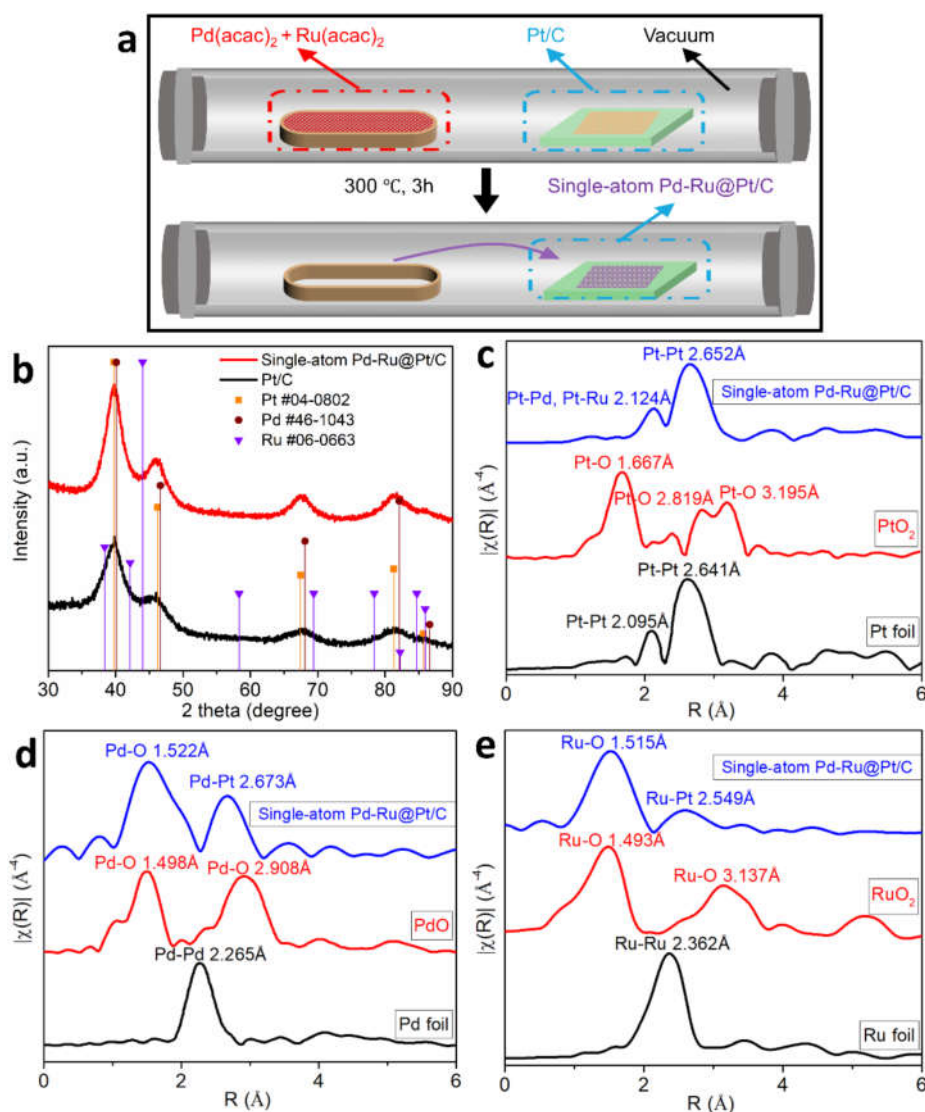


Fig. 2| Preparation and structure characterization of electrocatalysts. (a) Scheme for synthesizing single-atom Pd-Ru@Pt through a chemical vapor deposition (CVD) setup. **(b)** X-ray diffraction (XRD) pattern of single-atom Pd-Ru@Pt/C and Pt/C. **(c)** Pt, **(d)** Pd and **(e)** Ru Extended X-Ray Absorption Fine Structure (EXAFS) fitting results of single-atom Pd-Ru@Pt/C.

Single-atom Pd and Ru decoration on Pt for Pd-Ru@Pt/C catalysts was directly evidenced by extended X-ray absorption fine structure (EXAFS). The Pt EXAFS in Pd-Ru@Pt/C (**Fig. 2c**) displays a main peak at ~ 2.652 Å, which is close to that of the Pt–Pt bond length in bulk Pt (2.641 Å in Pt foil). Pt–Pd and Pt–Ru bonds at 2.124 Å are also observed in the EXAFS. However, no sign of Pd–Pd bond (2.265 Å) is observed in the Pd EXAFS (**Fig. 2d**) for the Pd-Ru@Pt/C catalyst. Additionally, a Pd–O peak at ~ 1.522 Å and a Pd–Pt peak at ~ 2.673 Å are observed. Similarly, no

Ru-Ru bond (2.362 Å) shows up in the Ru EXAFS (**Fig. 2e**), but a Ru-Pt peak at ~2.549 Å is featured. The first peak at 1.493 Å in the Ru EXAFS corresponds to the Ru-O bond. The observed Pd-O and Ru-O without Pt-O is consistent with a structure of single-atom Pd-Ru decoration on the Pt surface. Therefore, the EXAFS characterization confirmed the single-atom Pd-Ru doped Pt structure without the formation of Pd or Ru nanoparticles/clusters.

To further investigate the composition, the single-atom Pd-Ru@Pt/C catalyst was characterized using an energy-dispersive x-ray (EDX) spectroscopy elemental analysis and X-ray photoelectron spectroscopy (XPS). The EDX analysis shows that the atomic ratio of Pt:Ru:Pt is 1.0:0.3:0.3 in bulk (**Supplementary Table 1**), while the XPS gives an atomic ratio of 1.0:0.5:1.4 in the topmost layer (**Supplementary Fig. 6-9**, and **Supplementary Table 2**). The significant surface enrichment of both Pd and Ru confirms the surface doping on Pt surface, indicating that most Pd and Ru atoms are close together on top of the Pt surface.

Structure thermodynamic stability

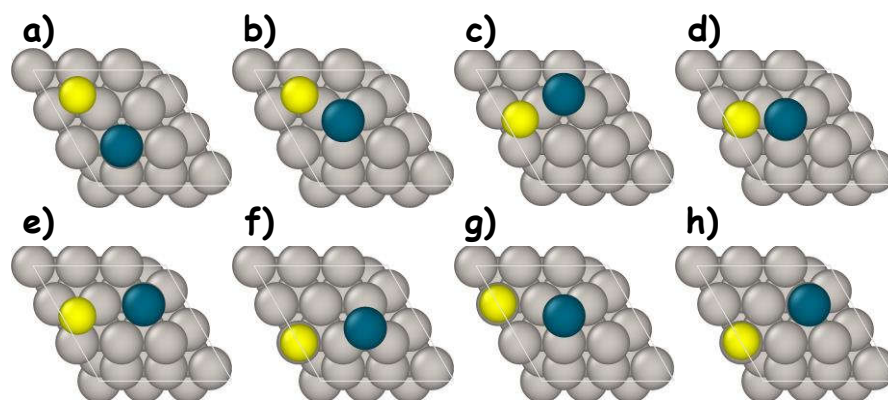


Fig. 3| Top view of the configurations simulated for Pd (dark green) and Ru (yellow) deposition on top of a Pt (111) surface (gray). Ru adsorbed at the hcp site and Pd adsorbed at the top site (**a**), Ru adsorbed at the hcp site and Pd adsorbed at the fcc site (**b**), Ru adsorbed at the fcc site and Pd adsorbed at the hcp site (**c**), Ru adsorbed at the fcc site and Pd adsorbed at the fcc site (**d**), Ru adsorbed at the fcc site and Pd adsorbed at the top site (**e**), Ru adsorbed at the top site and Pd adsorbed at the hcp site (**f**), Ru adsorbed at the top site and Pd adsorbed at the fcc site (**g**) and Ru adsorbed at the top site and Pd adsorbed at the top site (**h**).

In order to gain an atomic-level understanding of the dopant decoration, the preferred adsorption sites of the Pd and Ru atoms at the fcc, hcp, and top sites of the Pt (111) surface were analyzed from a thermodynamic standpoint using DFT calculations (**Fig. 3a-h**). The analysis was restricted to the adsorption of dopants in detriment of the absorption process. The ground state energy geometry found under vacuum conditions predicted that the optimized site for both Pd and Ru adsorption on top of the Pt (111) slab is the fcc site (**Fig. 3d**). This configuration is at least 0.4 eV more thermodynamically stable than the least preferred configuration of Ru adsorbing at a hollow fcc site and Pd adsorbing at a top site (**Fig. 3e**).

To explore whether the single Pd or single Ru atom prefers to deposit on the Pt (111) slab as a single-atom dopant or as a clustered dopant, we calculated the binding energy of a single-atom Pd (or Ru) dopant on the Pt (111) surface and the energy required to add a dopant once a single-atom Pd (or Ru) dopant was already adsorbed at an fcc site of the Pt (111) surface. The binding energy (E_{binding}) per atom (n) was calculated as the difference between the total energy of the optimized substrate-adsorbate and the sum of the relaxed clean surface (E_{slab}) and isolated dopants (E_{TM}).

$$E_{\text{binding}} = \frac{E_{\text{total}} - (E_{\text{slab}} + \sum n E_{\text{TM}})}{n} \quad \text{Eq. 1}$$

Upon optimization of the single-atom Pd (or Ru) adsorption on the Pt (111) surface, the binding energy of Pd-Pt (-2.77 eV) is larger than either of the Pd-Pd (-0.54 eV) and Pd-Ru (-1.07 eV) binding energy. Also, the binding energy of Ru-Pt (-5.47 eV) is also larger than either of the Ru-Ru (-2.80 eV) and Ru-Pd (-1.07 eV) binding energies. Therefore, both transition metals, Pd and Ru, prefer to form bonds with Pt atoms at the fcc site of the Pt (111) surface rather than forming clusters.

To further investigate the long-term single-atom Pd-Ru@Pt stability, the energetic cost of sequential dopant addition (assuming a Ru or Pd is already adsorbed at an Pt fcc site) was simulated. The energy required to add a Ru atom and form a Ru-Ru on the Pt surface is 1.30 eV/atom. The energy required to add a Pd atom and form a Pd-Pd on the Pt surface is 0.33 eV/atom. Meanwhile, the energy required to add a Pd atom and form a single-atom Ru and Pd dopants adsorbed at the Pt (111) surface is 0.09 eV/atom. Therefore, a single-atom Pd-Ru on the Pt surface is preferred over the clustering of Ru and Pd. In other words, using a single-atom Pd-Ru@Pt as a baseline, the agglomeration energy barriers of Pd and/or Ru on a Pt surface further stabilize the single-atom decoration system.

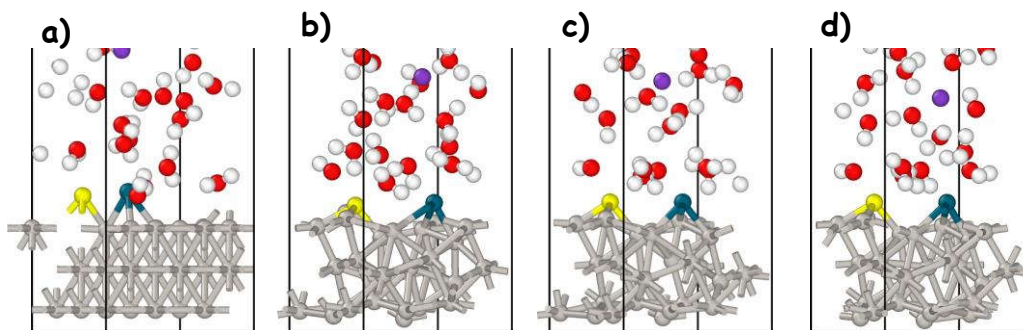


Fig. 4| Snapshots of the time evolution of the Pd-Ru@Pt (111) slab shown at a) the initial configuration, b) 6,000 fs, c) 12,000 fs and d) 18,000 fs. Color code: Gray, green, yellow, white, red, and purple spheres represent Pt, Pd, Ru, H, O, and K, respectively.

The thermodynamic stability of the Pd-Ru@Pt catalyst in an alkaline environment was investigated using AIMD simulations by an electrified Pt (111)/H₂O interface. As shown in **Fig. 4**, the Pd and Ru atoms continue to be adsorbed on the outermost surface of the Pt (111) catalyst with an elongated separation between the Pd and Ru atoms with respect to the initially optimized positions of ~ 2.6 Å. Indeed, AIMD simulations in an NVT ensemble at room temperature (constant

number of atoms, fixed volume, and controlled temperature) show that after approximately 18,000 fs of simulation time the Ru-Pd distance is close to 5 Å, confirming the single-atom pair stability in alkaline electrolyte.

Electronic structure

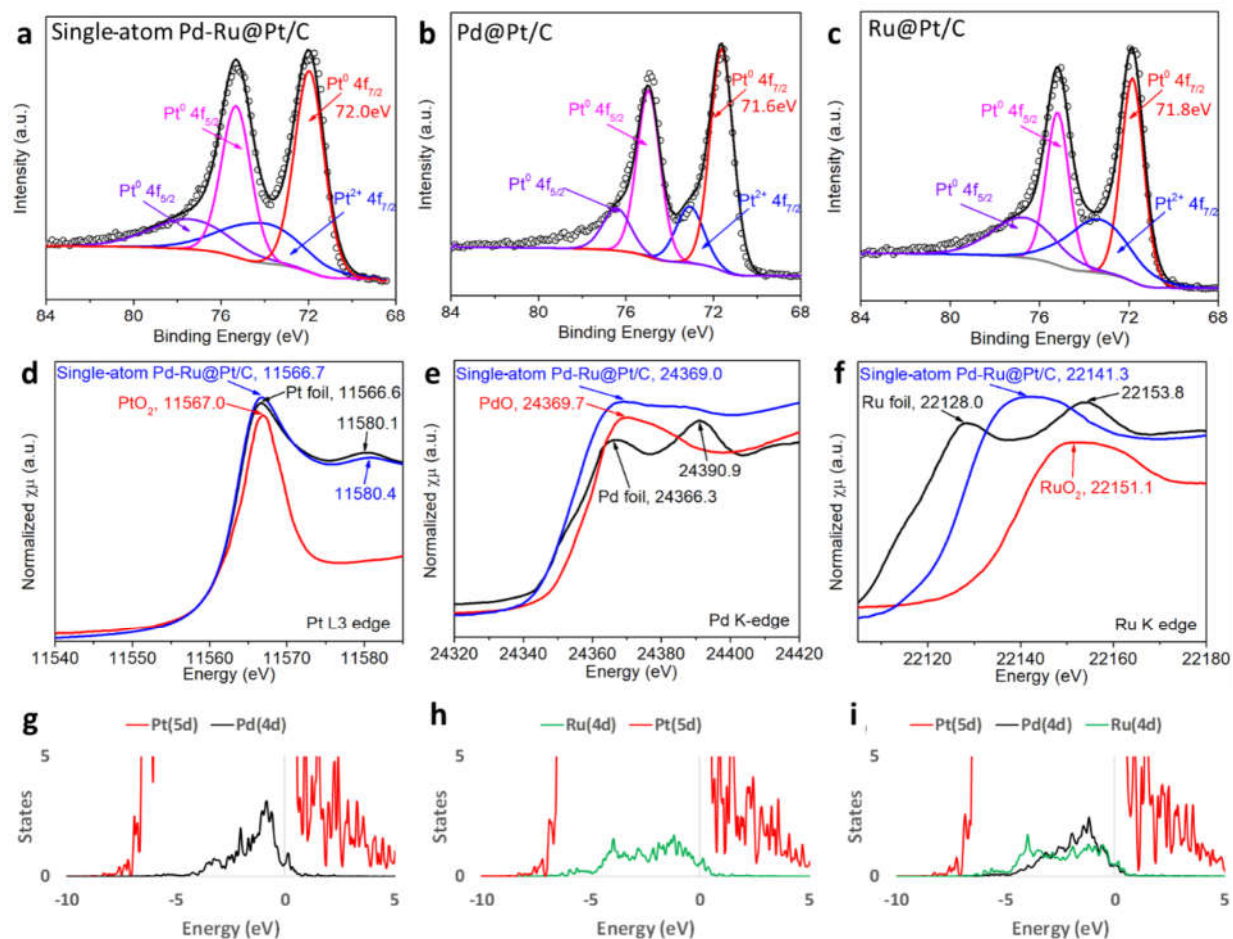


Fig. 5| Electronic structure characterization. XPS pattern of Pt 4f for (a) single-atom Pd-Ru@Pt/C, (b) Pd@Pt/C, and (c) Ru@Pt/C. (d) Pt L3-edge, (e) Pd K-edge, and (f) Ru K edge X-ray Absorption Near Edge Structure (XANES) spectra. XANES of metallic Pt and PtO₂ are shown in (d) as references¹². XANES of metallic Pd and PdO are shown in (e) as references¹³. XANES of metallic Ru and RuO₂ are shown in (f) as references¹⁴. Partial density of states (PDOS) for (g) Pd-doped system, (h) Ru-doped system, and (i) single-atom Pd-Ru@Pt (111) slab.

An XPS experiment was used to study the electronic effect of the dopant on Pt. The Pt⁰:Pt²⁺ ratio of Pd-Ru@Pt/C (4.1:1.0) from deconvoluted high-resolution Pt XPS spectra was considerably larger than either of Pd@Pt/C (3.3:1.0) and Ru@Pt/C (1.4:1.0) Pt⁰:Pt²⁺ ratio (Fig. 5c and Supplementary Table 3), which favors reactant activation on Pd-Ru@Pt/C. The higher Pt⁰ binding energy in Pd-Ru@Pt/C (72.0 eV) (Fig. 5a) than that in Pt/C (71.8 eV) (Supplementary Fig. 7a and Supplementary Table 3) enhances the HOR kinetics by the weakening hydrogen

adsorption on the surface.⁵ In contrast, the Pt⁰ binding energy in Pd@Pt/C negatively shifts to 71.6 eV (**Fig. 5b**) from 71.8 eV in Pt/C. The Ru-doping on Pt/C (**Fig. 5c**) does not change the Pt⁰ binding energy significantly, ruling out the electronic effect of Ru on the HOR performance for Ru@Pt/C.

Furthermore, the oxidation states of Pt, Pd, and Ru, were probed by the white line intensity in the XANES spectra. The Pt L3-edge white line intensity of Pd-Ru@Pt/C is close to that of Pt foil (**Fig. 5d**), indicating that the average oxidation state of Pt is primarily zero. However, the white line intensity of the Pd K-edge (**Fig. 5e**) from Pd-Ru@Pt/C features a combination of metallic Pd and PdO. For the Ru K edge (**Fig. 5f**), the energy absorption edge fell between those of metallic Ru foil and RuO₂, suggesting the co-existence of metallic and oxidized states.

In addition, the electronic structure signatures of the bare Pt (111) surface for Pd@Pt, Ru@Pt, and Pd-Ru@Pt were calculated using DFT. **Fig. 5g** shows that a valence band with additional occupied (*d*) states was detected for the Pd@Pt (111) surface model, these (*d*) states for Pd covers the higher region of the valence band, which extends from ~-3.6 eV up to the Fermi level (set at 0 eV). Similarly, more (*d*) states were found (**Fig. 5h**) at the Fermi level of the Ru@Pt (111) surface when compared to the pristine Pt (111) surface. Interestingly, Ru provides more (*d*) states deeper into the valence band while still contributing states closer to the Fermi level (**Fig. 5i**). Moreover, downshift of the (*d*) band center reduces the filling of anti-bonding states resulting in a weaker adsorbate-surface bond and hence beneficial impact on improving the HOR kinetics of Pt in alkaline media^{5, 15}. Based on DFT, the (*d*) band center down shifts from -2.01 eV on the pristine Pt (111) surface to -2.09 eV on the Ru@Pt (111) surface, to -2.16 eV on the Pd@Pt (111), and to -2.23 eV on the Pd-Ru@Pt (111) surface. The Pd-Ru@Pt (111) surface shows the greatest downward shift in the Pt (*d*) band center, corresponding to the weakest hydrogen adsorption strength on the surface, i.e. the smallest hydrogen binding energy (HBE) and the most favorable HOR performance.

Electrochemical performance

The effects of surface decoration on electrocatalytic behavior in electrolytes with different pH was explored using a rotating disk electrode (RDE) test in both 0.1M KOH and 0.1M HClO₄. **Supplementary Fig. 9a** confirms that the decreased HOR activities of Pt in alkaline electrolytes compared to that in acidic electrolytes is due to the increased HBE as evidenced by the 145mV positive shift of the hydrogen desorption peak in the cyclic voltammogram (CV)¹⁶. After the single-atom Pd-Ru co-doping on the Pt surface, the hydrogen desorption peak of the Pd-Ru@Pt/C in the alkaline electrolyte shifted negatively to 116 mV from 280 mV for the Pt/C (**Supplementary Fig. 9a-b**), which is even comparable to that of the Pd-Ru@Pt/C in acidic electrolytes (**Supplementary Fig. 9b**). In contrast, only Pd or Ru doping on a Pt surface does not shift the peak-current potential of Pt significantly in alkaline electrolytes (**Supplementary Fig. 9a, c-d**). In 0.1M KOH, the single-atom Pd-Ru co-doping on Pt negatively shifted the desorption peak potential indicating the weakened dissociated H_{ads} compared with the reference Pt/C (**Fig. 6a**),

which contributed to HOR performance improvement. The DFT calculations confirm that the Pd and Ru co-doping on Pt reduces the HBE to -0.42 eV, which is smaller than the HBE (-0.59 eV) of Pd-doped Pt catalysts. The optimization process snapshots of the single-atom Pd-Ru@Pt (Supplementary Fig. 10) shows that an H atom that originally adsorbs on top of the Pd atom moves to the Pt surface, validating efficient hydrogen spillover when using Pd in the presence of Ru dopants.

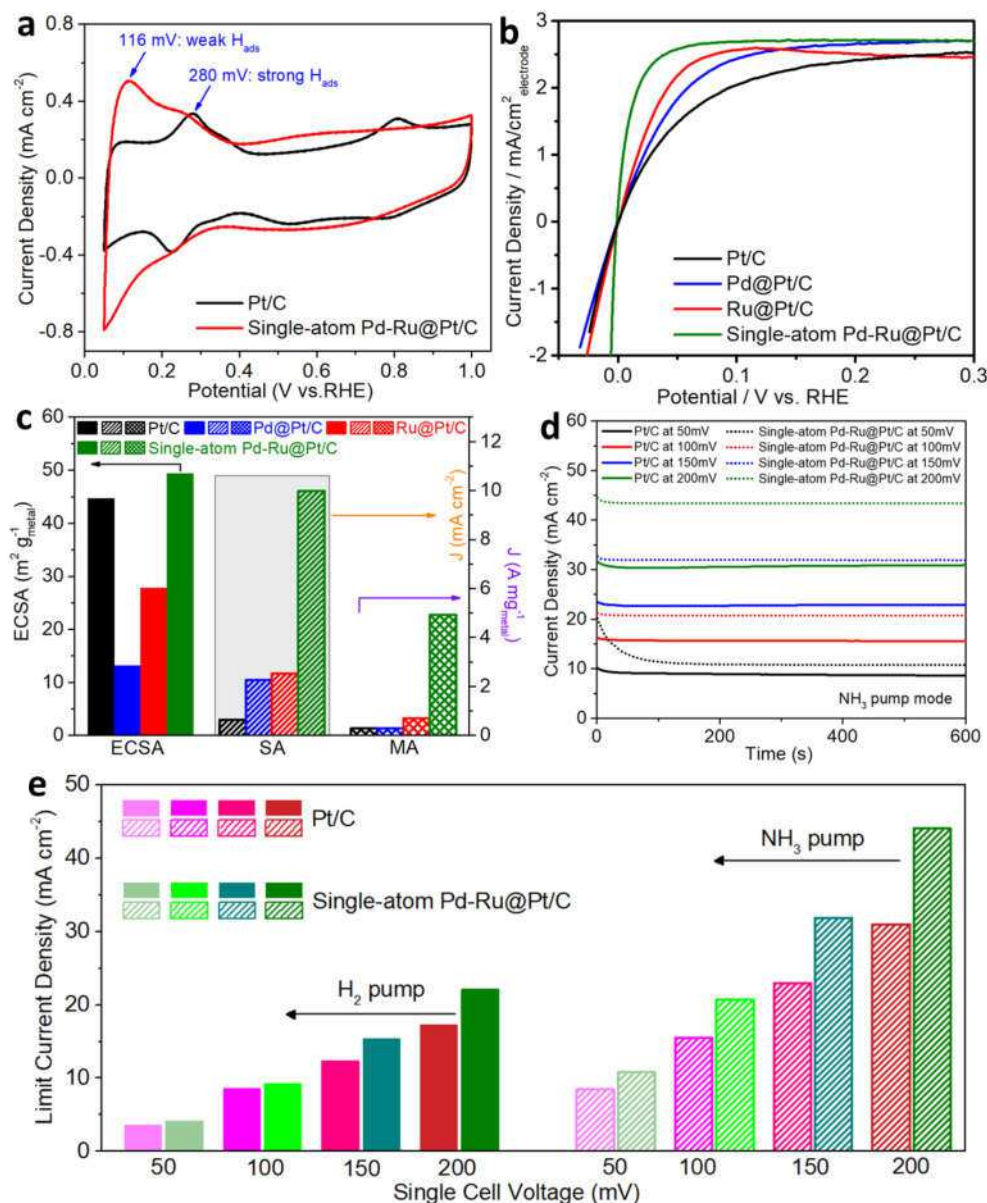


Fig. 6| Electrochemical performance and mechanism of different catalysts. (a) CV curves of different catalysts. Test condition: 0.05 to 1.00 V vs. RHE, 50 mV/s, N₂-saturated 0.1M KOH. (b) HOR polarization curves of different catalysts. Test condition: -0.05 to 0.40V vs. RHE, 10 mV s⁻¹, H₂-saturated 0.1M KOH, RDE at 1600 rpm. (c) Comparison of ECSA (black arrow, left axis), SA (normalized by ECSA, orange arrow, right axis) and MA (normalized by Pt mass, purple arrow,

right axis) for HER at 50 mV vs. RHE for all tested catalysts. (d) Gibbs Free energy profiles for catalysts at equilibrium potential and pH = 14. (e) Comparison of limit current density of Pt/C and single-atom Pd-Ru@Pt/C under H₂ pump and NH₃ pump mode in electrochemical cell. Test condition: Nafion 211 membrane, 5 cm² electrode, 25 °C, 34% relative humidity (RH) for H₂-NH₃ mixture, 0.2 bar H₂-NH₃ mixture at flow rates of 50 mL min⁻¹ of H₂ and 100 mL min⁻¹ of NH₃.

The HOR performances of Pd-Ru@Pt/C and other reference catalysts (Pt/C, Pd@Pt/C, and Ru@Pt/C) were evaluated using linear sweep voltammetry (LSV) in an N₂-saturated 0.1 M KOH electrolyte at a scan rate of 5 mV s⁻¹ (Fig. 6b). The ECSAs of catalysts in alkaline electrolytes were further determined by measuring the under-potential hydrogen deposition (H_{upd})⁷ for Pt/C (Supplementary Fig. 9a) or the under-potential copper deposition (Cu_{upd})¹⁷ for Pd or Ru doped Pt catalysts (Supplementary Fig. 12) since hydrogen can absorb into the Pd leading to over-estimated ECSA but only Cu monolayer absorbs on Pd surface. The single-atom Pd-Ru@Pt/C gave the highest ECSA of 49.3 m² g_{metal}⁻¹ among all other catalysts including the Pt/C (44.6 m² g_{metal}⁻¹), Pd@Pt/C (7.7 m² g_{metal}⁻¹), and Ru@Pt/C (27.7 m² g_{metal}⁻¹) (Fig. 6c). Therefore, decorating single-atom Pd-Ru on Pt/C increases the ECSA. To quantitatively compare the intrinsic HOR activity, the kinetic currents were obtained from the current-potential response of each catalyst (Supplementary Fig. 11a-d) using the Koutecký–Levich equation. As shown in the Koutecký–Levich plots (Supplementary Fig. 11e), the j⁻¹ intercept (1/j_k) of the Pd-Ru@Pt/C catalyst (green) is much smaller than those of other reference catalysts. The calculated j_k of the Pd-Ru@Pt/C catalyst is 20.2 mA cm⁻², which is 4.6 times higher than for the Pt/C (4.3 mA cm⁻²). Therefore, the HOR kinetics on the Pd-Ru@Pt surface is the quickest. The SA and MA of the single-atom Pd-Ru@Pt/C at 50 mV vs. RHE are 9.98 mA cm⁻² and 4.93 A mg⁻¹_{metal}, respectively. These activities are 15.9 and 17.5 times higher than those for the Pt/C, respectively (Fig. 6c). To our knowledge, such a high HOR activity reported here for the Pd-Ru@Pt/C in an alkaline solution has not been achieved by any other nanomaterial under comparable conditions. Furthermore, the exchange current densities are obtained using the Koutecký–Levich equation and the Butler–Volmer equation (Method part). From Supplementary Fig. 13 and Supplementary Table 4, the specific exchange current density of Pt/C was determined to be 0.29 mA cm⁻²_{Pt}, in agreement with previous report¹⁸. The specific exchange current density (1.61 mA cm⁻²_{Pt}) of single-atom Pd-Ru pair was 5.5 times that of the Pt/C (0.29 mA cm⁻²_{Pt}), 2.6 times of Pd@Pt/C (0.62 mA cm⁻²_{Pt}) and 1.8 times of Ru@Pt/C (0.88 mA cm⁻²_{Pt}). Normalized to metal mass, the mass exchange current density (0.79 mA mg⁻¹_{metal}) of single-atom Pd-Ru@Pt/C was 6.0 times that of the Pt/C (0.13 mA mg⁻¹_{metal}), 9.7 times that of Pd@Pt/C (0.08 mA mg⁻¹_{metal}) and 6.5 times that of Ru@Pt/C (0.12 mA mg⁻¹_{metal}). Therefore, either of Pd or Ru single-atom modification can only enhance the specific exchange current density of Pt, but it cannot improve the mass exchange current density of Pt. To contrast, the single-atom Pd-Ru pair effectively improves both the specific and mass exchange current density of Pt.

Moreover, the electrochemical durability of the Pd-Ru@Pt/C in an alkaline electrolyte was also assessed by accelerated stability tests between 0.05 and 0.4 V (vs. RHE) at 100 mV s⁻¹ in N₂-

saturated 0.1 M KOH. The CV curve was recorded every 2,000 cycles. The ECSA retains more than 95% of the initial value during the cycling process (**Supplementary Fig. 14**). Furthermore, the SA and MA of the Pd-Ru@Pt/C after 10,000 cycles were still much higher than those for the Pt/C (17.7 and 19.6 times, respectively) (**Supplementary Fig. 15-16**).

To reveal the HOR reaction mechanism, the Gibbs Free Energy profile at an equilibrium potential of -0.8 V with pH = 14 was calculated using DFT. The Gibbs Free energy profile (**Fig. 6d**) shows a more negative ΔG of H* for pristine Pt (111) when compared to both the Pd@Pt (111) and Pd-Ru@Pt (111) slabs. The H* oxidation is endothermic with the Pd-Ru@Pt (111) surface catalyst showing the smaller barrier for H* oxidation. The pristine Pt (111) catalyst has the highest thermodynamic free energy change value at an equilibrium potential for H* oxidation. Therefore, the barrier for H* oxidation decreases in the order: Pt (111) > Pd@Pt (111) > Pd-Ru@Pt (111). Following this discovery, the increased water adsorption strength on the Pd-Ru@Pt surface in alkaline electrolytes was validated by Fourier-transform infrared spectroscopy (FTIR). The relative absorbance of the OH stretching bands can be used to estimate the overall water organization changes. Water adsorption changes OH stretching modes in the region 3000–3500 cm^{-1} which are highly sensitive to water's hydrogen bond (HB) network. The broad band consists of two main components peaking at 3250 (ν_1) and 3400 cm^{-1} (ν_2), which relate to water molecules in tetrahedral-bonded ice-like organization and an HB-distorted liquid environment, respectively.¹⁹ The increase of the bands absorbance at 3250 cm^{-1} demonstrates a higher coordination of water molecules. As shown in **Supplementary Fig. 17**, the ratio R of $\nu_1 : \nu_2$ increases in the order: R(0.1M KOH) < R(Pt/C 0.1M KOH) < R(Pd-Ru@Pt/C 0.1M KOH), indicating the increased coordination and water-substance interaction strength. Furthermore, the ΔG of H₂O desorption on different catalysts was calculated, assuming 0 eV on a pristine Pt (111) surface as reference. Since the H₂O desorption is endothermic for both Pd-Ru and Pd doped catalysts, the Pd-Ru@Pt (111) surface showed the larger H₂O desorption barrier (0.45 eV) when compared to the Pd@Pt (111) surface (0.18 eV) (**Fig. 6d**). Therefore, both FTIR and simulation confirmed that H₂O has a stronger interaction with Pd-Ru@Pt (111), which in turn weakens the hydrogen binding and increases the HOR activity.

Additionally, the single-atom Pd-Ru@Pt/C increases the HER activity (**Supplementary Fig. 18-18**). As shown in **Supplementary Fig. 19a**, the overpotential of the Pd-Ru@Pt/C at 10 mA cm^{-2} is 32 mV less than that of the benchmark Pt/C. At 50 mV vs. RHE, the SA (1.59 mA cm^{-2}) and MA (0.78 A $\text{mg}^{-1}_{\text{metal}}$) of the Pd-Ru@Pt/C are double the Pt/C values (**Supplementary Fig. 19b**).

In a proof-of-principle demonstration of practical application, we compared the bifunctional hydrogen electrocatalytic activity of Pt/C and Pd-Ru@Pt/C using a 5 cm^2 H₂ pump cell and NH₃ pump cell (**Supplementary Fig. 20**). The Pd-Ru@Pt/C delivered 1.2 times steady current density than the Pt/C in the H₂ pump mode (**Supplementary Fig. 21**), indicating enhanced HOR and HER performance in acidic environments. The Pd-Ru@Pt/C also showed a 1.4 times higher steady current value than the Pt/C in the NH₃ pump mode in alkaline environments (**Supplementary Fig. 22 and Fig. 6e**), which is consistent with the advantage of optimized surface micro-environments

via single-atom Pd-Ru doping in the presence of OH⁻. The remarkable HOR and HER performance of the Pd-Ru@Pt/C is further demonstrated in the high pressure NH₃ compression mode, as shown in **Supplementary Fig. 23**.

Conclusion

Single-atom Pd-Ru decoration on Pt nanoparticles (single-atom Pd-Ru@Pt) was synthesized by trapping the high-temperature-evaporated Pd and Ru atoms from precursors onto the Pt nanoparticle surface. The stable single-atom Pd-Ru@Pt structure is verified by both EXAFS and DFT simulations. The SA and MA of the single-atom Pd-Ru@Pt/C for the HOR are 9.98 mA cm⁻² and 4.93 A mg⁻¹_{metal}, which are 15.9 and 17.5 times higher than that of the state-of-the-art Pt/C, respectively. For the HER, the SA (1.59 mA cm⁻²) and MA (0.78 A mg⁻¹_{metal}) of the single-atom Pd-Ru@Pt/C are also twice as high as that of the Pt/C. DFT shows that the dopants modify the electronic structure of the Pt (111) surface by changing the states near the Fermi level and shifting the (*d*) band center of the outermost Pt atoms further away from the Fermi level, effectively weakening hydrogen chemisorption strength. Moreover, DFT and AIMD simulations show the continued dopant stability and preferred adsorption mode in the presence of a liquid environment as well as the efficiency of the hydrogen spillover in the presence of co-dopants. Practically, the enhanced HOR and HER performances of the single-atom Pd-Ru@Pt/C is validated by NH₃ and H₂ electrochemical pump performance. The demonstrated electrochemical device can easily be scaled up on demand. With renewable energy as the power input, our method represents an efficient, distributed, and sustainable NH₃ and H₂ separation and/or compression with broad scientific and technical impacts.

Methods

Synthesis of electrocatalysts. All chemicals were purchased from Sigma-Aldrich unless otherwise specified. Pt nanoparticles supported on carbon black were prepared via a solvothermal technique following previously reported procedures²⁰. Typically, 2.5 mL of H₂PtCl₆ solution (40 mM in ethylene glycol (EG)) was added into 60 mL EG. The pH of the solution was adjusted to 12 by adding 1 M NaOH in EG. Then, 80 mg of carbon black was added to the above solution and stirred for 1 h. The solution was heated at 120 °C for 4 h. After cooling down, the pH of the reaction solution was adjusted to < 3 using 2 M HNO₃ aqueous solution, then 40 mL water was added and stirred for 10 h. The resulting catalyst was washed with DI water until Cl⁻ was not detected by silver nitrate titration method and then vacuum dried overnight at 80 °C, denoted as Pt/C.

Atomic Pd-Ru doped Pt/C was synthesized by the catalytic pyrolysis method. In detail, 2.5 mg of Ru(acac)₃ and 2.5 mg of Pd(acac)₂ were mixed and transferred into a combustion boat, which was transferred to a glass tube. A silicon wafer with 20 mg of Pt/C was put into the tube. Then the tube was sealed under vacuum and underwent thermal treatment before being cooled to room temperature in the tube furnace. Thermal treatment detail: Increase temperature from 30°C to 300°C

over 2h and hold at 300°C for 60 min. Pd or Ru doped Pt/C was obtained using similar procedure, except that 5 mg Ru(acac)₂ or Pd(acac)₂ was used instead of bi-salt mixture.

Material characterizations. The catalyst morphology was characterized by a JEOL 2100F field emission TEM with an electron accelerating voltage of 200 keV. EDS was obtained on a Hitachi SU-70 FEG SEM coupled with a Bruker EDS system. The X-ray diffraction (XRD) was conducted with a Bruker D8 X-ray diffractometer (Cu K α radiation, $\lambda = 1.5418 \text{ \AA}$). X-ray photoelectron spectroscopy (XPS) was performed on a high sensitivity Kratos Axis 165 X-ray photoelectron spectrometer equipped with Mg K α radiation. The binding-energy was calibrated using the C 1s peak of carbon at 284.8 eV. Fourier transform infrared spectroscopy (FTIR) was recorded by a NEXUS 670 FT-IR Instrument. XAS measurements were performed at the 7-BM beamline of the National Synchrotron Light Source II (NSLS II) at Brookhaven National Laboratory in the transmission mode. The X-ray absorption near edge structure and Extended X-ray absorption fine structure spectra were processed using the Athena software package. The AUTOBK code was used to normalize the absorption coefficient, and separate the EXAFS signal, $\chi(k)$, from the isolate atom-absorption background. The extracted EXAFS signal, $\chi(k)$, was weighted by k^3 to emphasize the high-energy oscillations and then Fourier-transformed in a k range from 3.0 to 10.5 \AA^{-1} to analyze the data in R space.

Electrochemical measurements for the HOR and HER. To prepare the catalyst ink, 5 mg catalyst and 20 μL 5wt% Nafion 117 solution were dispersed in 2.5 mL ethanol. Then, 4 μL ink was drop-cast on a glassy carbon electrode (0.196 cm^2) for the RDE test. A mercury/mercury oxide electrode was utilized as the reference electrode, with a graphite rod as the counter electrode. Cyclic voltammetry (CV) was performed in a N₂-saturated 0.1 M KOH electrolyte with a potential scan rate of 50 mVs^{-1} . The electrochemical active surface area (ECSA) of Pt/C was determined by integrating the hydrogen adsorption charge on the CV curve by assuming 210 $\mu\text{C}/\text{cm}^2$ for the adsorption of a hydrogen monolayer. All of the other catalyst ECSAs were obtained by means of copper underpotential deposition (Cu_{upd}). For the Cu underpotential deposition/stripping experiments, an N₂-saturated solution containing 2 mM CuSO₄ and 0.05 M H₂SO₄ was used as the electrolyte. For single-atom Pd-Ru@Pt/C and Ru@Pt/C, the electrode potential was first held at 0.95 V to oxidize all Ru sites. For other catalysts, there was no need to hold the electrode potential at 0.95 V before Cu_{upd}. The potential was held at 0.3 V versus RHE for 300 s to form a Cu_{upd} monolayer, and then followed by a linear scan to 0.95 V at 5 mV s^{-1} . The ECSAs were calculated by subtracting the background CVs that were collected in the N₂-saturated 0.05 M H₂SO₄ at 5 mV s^{-1} , assuming a charge density of 470 $\mu\text{C cm}^{-2}$. The HOR and HER tests were conducted with a working glassy carbon electrode rotation speed of 1,600 rpm in an H₂-saturated 0.1M KOH electrolyte with a potential scan rate of 10 mVs^{-1} . Accelerated durability tests were conducted by cycling between 0.05 V and 0.4 V versus RHE at 100 mV s^{-1} in N₂-saturated 0.1M KOH.

The kinetic current density (j_k) was obtained using the Koutecky–Levich equation (Eq. 2):

$$\frac{1}{j} = \frac{1}{j_d} + \frac{1}{j_k} \quad \text{Eq. 2}$$

where j was the measured current density ($\text{mA cm}^{-2}_{\text{electrode}}$), j_k was the kinetic current density ($\text{mA cm}^{-2}_{\text{electrode}}$), and j_d was the diffusion limit current density ($\text{mA cm}^{-2}_{\text{electrode}}$).

The exchange current densities (j_0) was obtained by fitting j_k to the Butler–Volmer equation (Eq. 3):

$$j_k = j_0 A_{rf} \left[e^{\frac{\alpha F}{RT} \eta} - e^{-\frac{(1-\alpha)F}{RT} \eta} \right] \quad \text{Eq. 3}$$

where j_0 was the exchange current densities ($\text{mA cm}^{-2}_{\text{Pt}}$), A_{rf} is the roughness factor, defined as the ratio between the electrochemical surface area and the geometric area of the disk ($\text{cm}^2_{\text{Pt cm}^{-2}_{\text{electrode}}}$), α is the transfer coefficient, F was the Faraday constant (96485 C mol^{-1}), R was the universal gas constant ($8.314 \text{ J mol}^{-1} \text{ K}^{-1}$), T was the absolute temperature (K), and η is the overpotential (V).

Electrochemical measurements for H₂ pump and NH₃ pump. Both the cathode and anode catalyst loading were $0.2 \text{ mg}_{\text{metal cm}^{-2}}$ for Pt/C and single-atom Pd-Ru@Pt/C. For the H₂ pump, a Nafion 211 membrane was used with 5 cm^2 active area operated at $25 \text{ }^\circ\text{C}$, 76% relative humidity (RH), and 0.2 bar of H₂ at a flow rate of 50 mL min^{-1} of H₂. For the NH₃ pump, a Nafion 211 membrane was used with 5 cm^2 active area operated at $25 \text{ }^\circ\text{C}$, 34% relative humidity (RH), and 0.2 bar for an H₂–NH₃ mixture at flow rates of 50 mL min^{-1} of H₂ and 200 mL min^{-1} of NH₃.

Computational Details. Density functional theory (DFT) calculations were performed using the Vienna *ab-initio* simulation package (VASP) code^{21,22} with the projector augmented wave (PAW) pseudopotentials²³. Generalized gradient approximation (GGA) of Perdew–Burke–Ernzerhof (PBE) functionals were used to implement electron exchange–correlation interactions with a kinetic energy cutoff of 400 eV ²⁴. The self-consistent field (SCF) and geometry convergence tolerance were set to 1×10^{-4} and $1 \times 10^{-3} \text{ eV}$, respectively. For geometry optimization calculations, a Γ -point-centered Monkhorst–Pack reciprocal grid of $5 \times 5 \times 1$ k-points was used for first Brillouin zone sampling. Meanwhile, a Γ -point was used for *ab-initio* molecular dynamics (AIMD) simulations at room temperature. The room temperature was maintained using Nosé–Hoover chains²⁵, with configurations belonging to the canonical (N, V, T) ensemble with a time step set to 1 fs. To mimic the water environment, the Amorphous Cell module from Materials Studio was used to pack the water molecules on top of the Pt (111) surface at a 1 g/cc density. To represent an alkaline environment, K^+ and OH^- species were introduced in the bulk of the water region. To explicitly include electric fields (0.2 V/\AA) in the calculations, a vacuum space greater than 10 \AA was introduced in the normal direction on top of the water molecules. The method by Neugebauer et al.²⁶ and improved by Feibelman²⁷ was used to explicitly include electric fields. The van der Waals (vdW) interaction was described with DFT-D3 method.²⁸ We used quantum-based electronic descriptors such as partial density of states (PDOS), obtained using the LOBSTER (Local Orbital Basis Suite Towards Electronic-Structure Reconstruction) program²⁹, to measure the interacting nature of atomic orbital pairs.

In order to model the Pt surfaces, a Pt slab cleaved along the (111) facet for five-layer slabs and three-layer slabs were used for geometry optimization calculations and AIMD simulations,

respectively. For the five-layer slab calculations, the top three layers in each slab were sufficiently relaxed in the calculations, whereas the bottom two layers were fixed at their bulk configurations. In order to avoid the computational cost of a five-layer slab, AIMD simulations were carried out on a reduced three-layer surface slab model. Calculations of hydrogen binding energies (ΔE_{HBE}) were performed according to the following equation:

$$\Delta E_{HBE} = E_{TOT}(\text{Pt slab} + \text{adsorbed species}) - E_{\text{Slab}}(\text{Pt slab}) - E_{\text{Species}} \frac{1}{2}(\text{H}_2) \quad \text{Eq. 2}$$

Here, E_{TOT} (Pt slab + adsorbed species) is the total energy of the system. Then, E_{Slab} (Pt slab) and E_{Species} (H_2) are the energies of the Pt(111) slab and the H_2 molecule, respectively. Calculation of the H_2 molecule was obtained by placing the atom in a 1 nm cube. To obtain the Gibbs Free Energy profiles of the HOR at 0 V and equilibrium potential, we followed the thermodynamic pathways of the HOR as described in the work of Wei and co-workers³⁰. The Open Visualization Tool (OVITO)³¹ was used to visualize all the configurations and models.

Reference

1. Durst, J.; Siebel, A.; Simon, C.; Hasché, F.; Herranz, J.; Gasteiger, H. A. New insights into the electrochemical hydrogen oxidation and evolution reaction mechanism. *Energy & Environmental Science* **2014**, 7, (7), 2255-2260.
2. Sheng, W.; Zhuang, Z.; Gao, M.; Zheng, J.; Chen, J. G.; Yan, Y. Correlating hydrogen oxidation and evolution activity on platinum at different pH with measured hydrogen binding energy. *Nature Communications* **2015**, 6, 5848.
3. Strmcnik, D.; Uchimura, M.; Wang, C.; Subbaraman, R.; Danilovic, N.; van der Vliet, D.; Paulikas, A. P.; Stamenkovic, V. R.; Markovic, N. M. Improving the hydrogen oxidation reaction rate by promotion of hydroxyl adsorption. *Nature Chemistry* **2013**, 5, 300.
4. Tao, Y.; Gibbons, W.; Hwang, Y.; Radermacher, R.; Wang, C. Electrochemical ammonia compression. *Chemical Communications* **2017**, 53, (41), 5637-5640.
5. Scofield, M. E.; Zhou, Y.; Yue, S.; Wang, L.; Su, D.; Tong, X.; Vukmirovic, M. B.; Adzic, R. R.; Wong, S. S. Role of Chemical Composition in the Enhanced Catalytic Activity of Pt-Based Alloyed Ultrathin Nanowires for the Hydrogen Oxidation Reaction under Alkaline Conditions. *ACS Catalysis* **2016**, 6, (6), 3895-3908.
6. Schwammlein, J. N.; El-Sayed, H. A.; Stuhmeier, B. M.; Wagenbauer, K. F.; Dietz, H.; Gasteiger, H. A. Origin of Superior Activity of Ru@Pt Core-Shell Nanoparticles towards Hydrogen Oxidation in Alkaline Media. *ECS Transactions* **2016**, 75, (14), 971-982.
7. Li, M.; Duanmu, K.; Wan, C.; Cheng, T.; Zhang, L.; Dai, S.; Chen, W.; Zhao, Z.; Li, P.; Fei, H.; Zhu, Y.; Yu, R.; Luo, J.; Zang, K.; Lin, Z.; Ding, M.; Huang, J.; Sun, H.; Guo, J.; Pan, X.; Goddard, W. A.; Sautet, P.; Huang, Y.; Duan, X. Single-atom tailoring of platinum nanocatalysts for high-performance multifunctional electrocatalysis. *Nature Catalysis* **2019**, 2, (6), 495-503.
8. Subbaraman, R.; Tripkovic, D.; Strmcnik, D.; Chang, K.-C.; Uchimura, M.; Paulikas, A. P.; Stamenkovic, V.; Markovic, N. M. Enhancing Hydrogen Evolution Activity in Water Splitting by Tailoring Li^+ -Ni(OH)₂-Pt Interfaces. *Science* **2011**, 334, (6060), 1256.
9. Zhang, J.; Sasaki, K.; Sutter, E.; Adzic, R. R. Stabilization of Platinum Oxygen-Reduction Electrocatalysts Using Gold Clusters. *Science* **2007**, 315, (5809), 220-222.
10. Cao, L.; Zhang, G.; Jiang, S.; Tang, X.; Qin, X.; Guo, X.; Shao, Z.; Yi, B. Enhancing the Oxygen Reduction Reaction Performance by Modifying the Surface of Platinum Nanoparticles. *ChemElectroChem* **2016**, 3, (2), 309-317.

11. Qu, Y.; Li, Z.; Chen, W.; Lin, Y.; Yuan, T.; Yang, Z.; Zhao, C.; Wang, J.; Zhao, C.; Wang, X.; Zhou, F.; Zhuang, Z.; Wu, Y.; Li, Y. Direct transformation of bulk copper into copper single sites via emitting and trapping of atoms. *Nature Catalysis* **2018**, *1*, (10), 781-786.
12. Zhu, Y.; Cao, T.; Cao, C.; Luo, J.; Chen, W.; Zheng, L.; Dong, J.; Zhang, J.; Han, Y.; Li, Z.; Chen, C.; Peng, Q.; Wang, D.; Li, Y. One-Pot Pyrolysis to N-Doped Graphene with High-Density Pt Single Atomic Sites as Heterogeneous Catalyst for Alkene Hydrosilylation. *ACS Catalysis* **2018**, *8*, (11), 10004-10011.
13. He, P.; Xu, B.; Xu, X.; Song, L.; Wang, X. Surfactant encapsulated palladium-polyoxometalates: controlled assembly and their application as single-atom catalysts. *Chemical Science* **2016**, *7*, (2), 1011-1015.
14. Wang, Z.; Xu, S.-M.; Xu, Y.; Tan, L.; Wang, X.; Zhao, Y.; Duan, H.; Song, Y.-F. Single Ru atoms with precise coordination on a monolayer layered double hydroxide for efficient electrooxidation catalysis. *Chemical Science* **2019**, *10*, (2), 378-384.
15. Mercer, M. P.; Hoster, H. E. Electrochemical Kinetics: a Surface Science-Supported Picture of Hydrogen Electrochemistry on Ru(0001) and Pt/Ru(0001). *Electrocatalysis* **2017**, *8*, (6), 518-529.
16. Sheng, W.; Zhuang, Z.; Gao, M.; Zheng, J.; Chen, J. G.; Yan, Y. Correlating hydrogen oxidation and evolution activity on platinum at different pH with measured hydrogen binding energy. *Nature Communications* **2015**, *6*, (1), 5848.
17. Wang, Y.; Wang, G.; Li, G.; Huang, B.; Pan, J.; Liu, Q.; Han, J.; Xiao, L.; Lu, J.; Zhuang, L. Pt-Ru catalyzed hydrogen oxidation in alkaline media: oxophilic effect or electronic effect? *Energy & Environmental Science* **2015**, *8*, (1), 177-181.
18. Schmidt, T. J.; Ross, P. N.; Markovic, N. M. Temperature dependent surface electrochemistry on Pt single crystals in alkaline electrolytes: Part 2. The hydrogen evolution/oxidation reaction. *Journal of Electroanalytical Chemistry* **2002**, 524-525, 252-260.
19. Petit, T.; Puskar, L.; Dolenko, T.; Choudhury, S.; Ritter, E.; Burikov, S.; Laptinskiy, K.; Brzustowski, Q.; Schade, U.; Yuzawa, H.; Nagasaka, M.; Kosugi, N.; Kurzyp, M.; Venerosy, A.; Girard, H.; Arnault, J.-C.; Osawa, E.; Nunn, N.; Shenderova, O.; Aziz, E. F. Unusual Water Hydrogen Bond Network around Hydrogenated Nanodiamonds. *The Journal of Physical Chemistry C* **2017**, *121*, (9), 5185-5194.
20. Zhang, S.; Shao, Y.; Yin, G.; Lin, Y. Carbon nanotubes decorated with Pt nanoparticles via electrostatic self-assembly: a highly active oxygen reduction electrocatalyst. *Journal of Materials Chemistry* **2010**, *20*, (14), 2826-2830.
21. Kresse, G.; Hafner, J. Ab initio molecular dynamics for liquid metals. *Physical Review B* **1993**, *47*, (1), 558-561.
22. Kresse, G.; Furthmüller, J. Efficiency of ab-initio total energy calculations for metals and semiconductors using a plane-wave basis set. *Computational Materials Science* **1996**, *6*, (1), 15-50.
23. Blöchl, P. E. Projector augmented-wave method. *Physical Review B* **1994**, *50*, (24), 17953-17979.
24. Perdew, J. P.; Burke, K.; Ernzerhof, M. Generalized Gradient Approximation Made Simple. *Physical Review Letters* **1996**, *77*, (18), 3865-3868.
25. Martyna, G. J.; Klein, M. L.; Tuckerman, M. Nosé-Hoover chains: The canonical ensemble via continuous dynamics. *The Journal of Chemical Physics* **1992**, *97*, (4), 2635-2643.
26. Neugebauer, J.; Scheffler, M. Adsorbate-substrate and adsorbate-adsorbate interactions of Na and K adlayers on Al(111). *Physical Review B* **1992**, *46*, (24), 16067-16080.
27. Feibelman, P. J. Surface-diffusion mechanism versus electric field: Pt/Pt(001). *Physical Review B* **2001**, *64*, (12), 125403.
28. Grimme, S.; Antony, J.; Ehrlich, S.; Krieg, H. A consistent and accurate ab initio parametrization of density functional dispersion correction (DFT-D) for the 94 elements H-Pu. *The Journal of Chemical Physics* **2010**, *132*, (15), 154104.
29. Maintz, S.; Deringer, V. L.; Tchougréeff, A. L.; Dronskowski, R. LOBSTER: A tool to extract chemical bonding from plane-wave based DFT. *Journal of Computational Chemistry* **2016**, *37*, (11), 1030-1035.

30. Feng, Z.; Li, L.; Zheng, X.; Li, J.; Yang, N.; Ding, W.; Wei, Z. Role of Hydroxyl Species in Hydrogen Oxidation Reaction: A DFT Study. *The Journal of Physical Chemistry C* **2019**, 123, (39), 23931-23939.
31. Stukowski, A. Visualization and analysis of atomistic simulation data with OVITO—the Open Visualization Tool. *Modelling and Simulation in Materials Science and Engineering* **2009**, 18, (1), 015012.

Acknowledgement

L. Cao and C. Wang at the University of Maryland gratefully acknowledge funding support from the Advanced Research Projects Agency–Energy under Contract No. DEAR0000962. E. Hu and X.-Q. Yang at Brookhaven National Laboratory (BNL) were supported by the Assistant Secretary for Energy Efficiency and Renewable Energy, Vehicle Technology Office of the U.S. Department of Energy through the Advanced Battery Materials Research (BMR) Program under contract DE-SC0012704. This research used beamlines 7-BM of the National Synchrotron Light Source II, a U.S. DOE Office of Science User Facility operated for the DOE Office of Science by Brookhaven National Laboratory under Contract No. DE-SC0012704. Computational resources from Texas A&M Supercomputing Center and from Texas Advanced Computing Center at UT Austin are gratefully acknowledged.

Author contributions

L. Cao, F. Soto, and D. Li conceived the idea. L. Cao and D. Li performed the electrochemical experiments. L. Cao synthesized the catalysts. L. Cao, D. Li, and T. Deng carried out characterizations. E. Hu, and X.-Q. Yang performed and analyzed EXAFS and XANES analysis. F. Soto and P. Balbuena proposed the mechanism research and simulations. All authors contributed to writing of the manuscript.

Competing interests

The authors declare no competing interests.

Figures

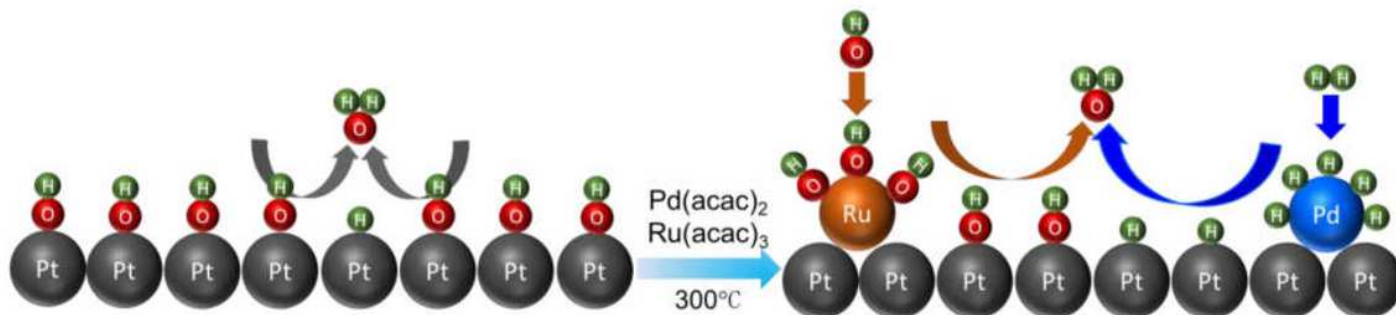


Figure 1

Hydrogen oxidation reaction schematic diagram on Pt and single-atom Pd-Ru@Pt surface. The decoration of Pt nanoparticles with paired single-atom Pd-Ru species increases the availability of H_{ads} and OH_{ads} on the Pt surface to boost the specific catalytic activity for the HOR without sacrificing the ECSA.

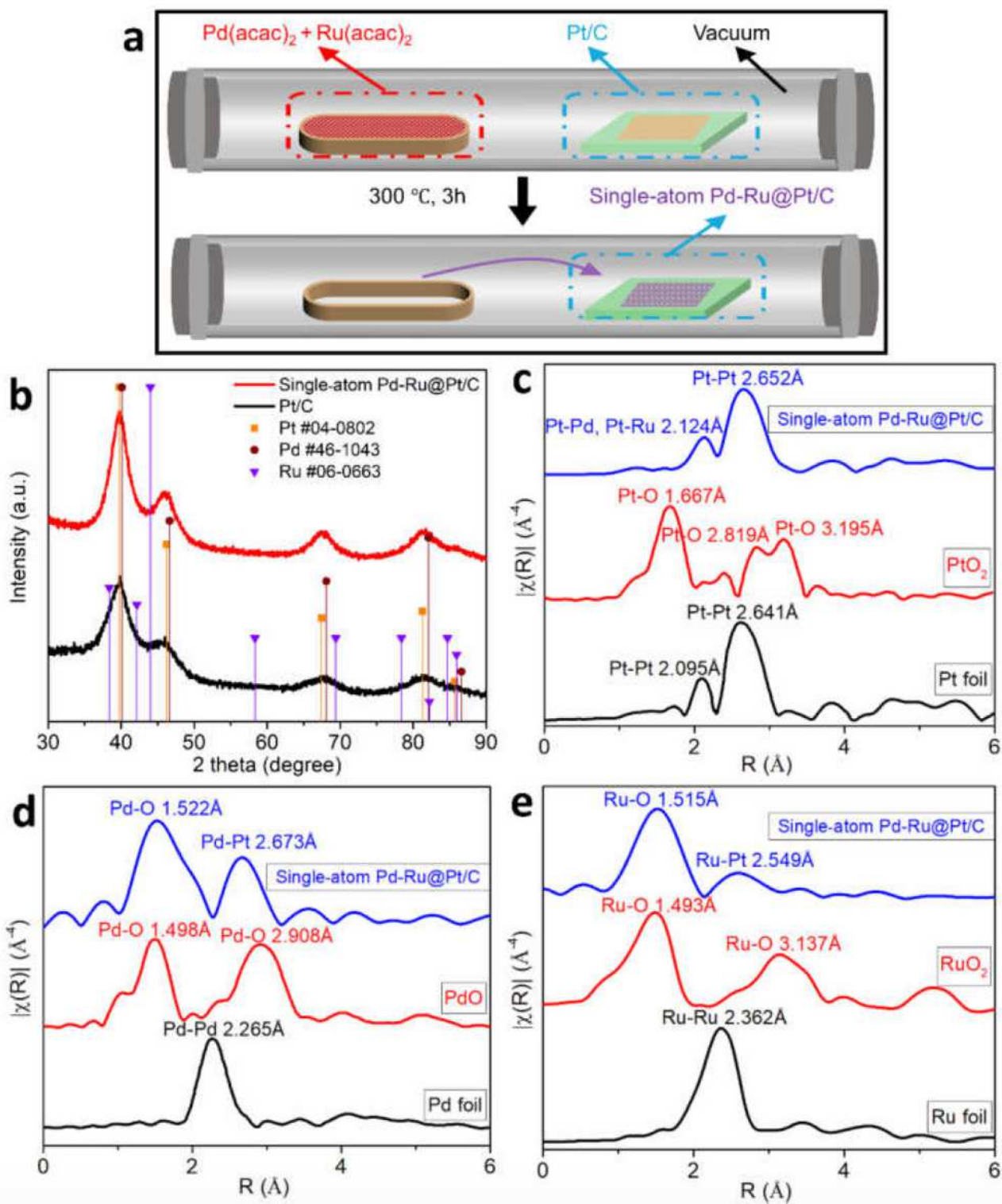


Figure 2

Preparation and structure characterization of electrocatalysts. (a) Scheme for synthesizing single-atom Pd-Ru@Pt through a chemical vapor deposition (CVD) setup. (b) X-ray diffraction (XRD) pattern of single-atom Pd-Ru@Pt/C and Pt/C. (c) Pt, (d) Pd and (e) Ru Extended X-Ray Absorption Fine Structure (EXAFS) fitting results of single-atom Pd-Ru@Pt/C.

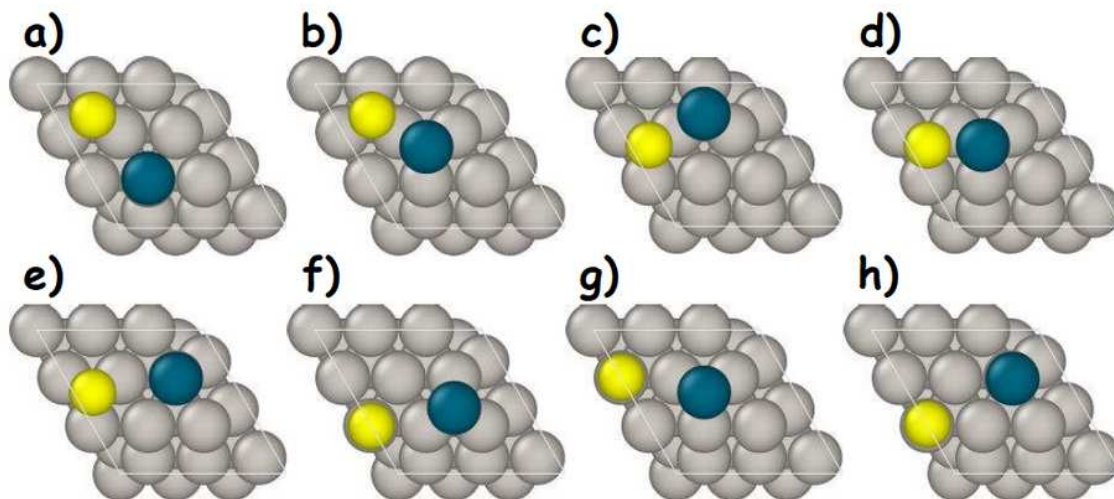


Figure 3

Top view of the configurations simulated for Pd (dark green) and Ru (yellow) deposition on top of a Pt (111) surface (gray). Ru adsorbed at the hcp site and Pd adsorbed at the top site (a), Ru adsorbed at the hcp site and Pd adsorbed at the fcc site (b), Ru adsorbed at the fcc site and Pd adsorbed at the hcp site (c), Ru adsorbed at the fcc site and Pd adsorbed at the fcc site (d), Ru adsorbed at the fcc site and Pd adsorbed at the top site (e), Ru adsorbed at the top site and Pd adsorbed at the hcp site (f), Ru adsorbed at the top site and Pd adsorbed at the fcc site (g) and Ru adsorbed at the top site and Pd adsorbed at the top site (h).

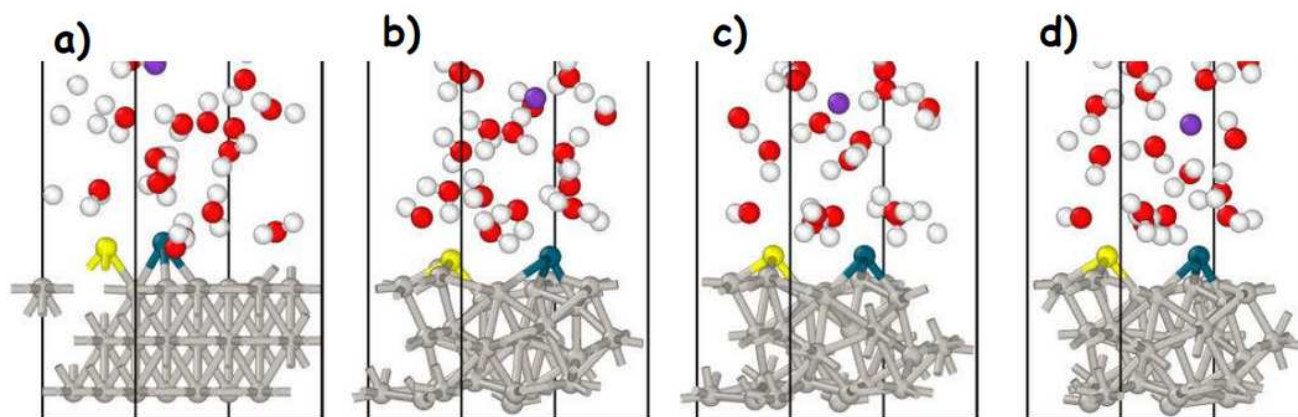


Figure 4

Snapshots of the time evolution of the Pd-Ru@Pt(111) slab shown at a) the initial configuration, b) 6,000 fs, c) 12,000 fs and d) 18,000 fs. Color code: Gray, green, yellow, white, red, and purple spheres represent Pt, Pd, Ru, H, O, and K, respectively.

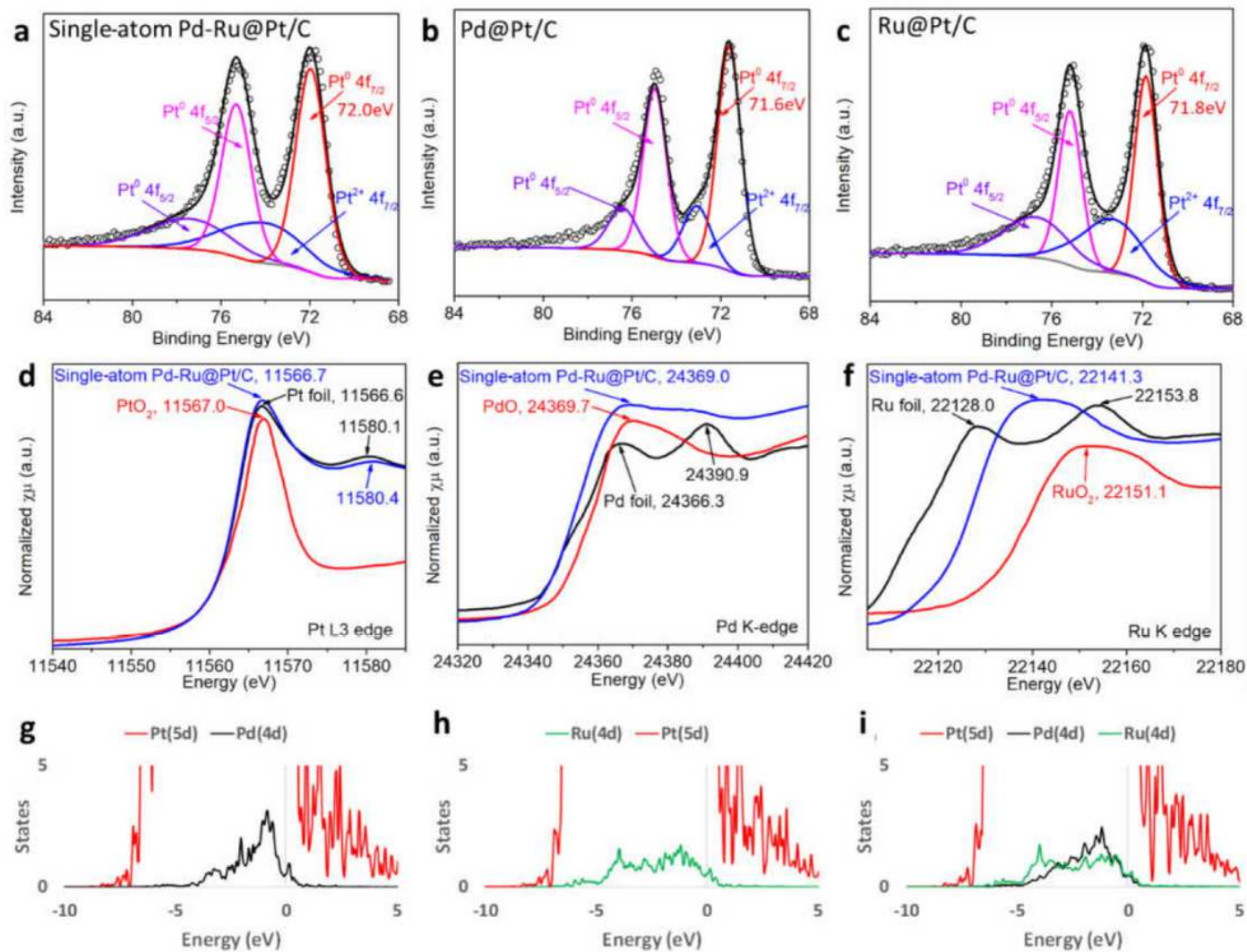


Figure 5

Electronic structure characterization. XPS pattern of Pt 4f for (a) single-atom Pd- Ru@Pt/C, (b) Pd@Pt/C, and (c) Ru@Pt/C. (d) Pt L3-edge, (e) Pd K-edge, and (f) Ru K edge X-ray Absorption Near Edge Structure (XANES) spectra. XANES of metallic Pt and PtO₂ are shown in (d) as references¹². XANES of metallic Pd and PdO are shown in (e) as references¹³. XANES of metallic Ru and RuO₂ are shown in (f) as references¹⁴. Partial density of states (PDOS) for (g) Pd-doped system, (h) Ru-doped system, and (i) single-atom Pd-Ru@Pt (111) slab.

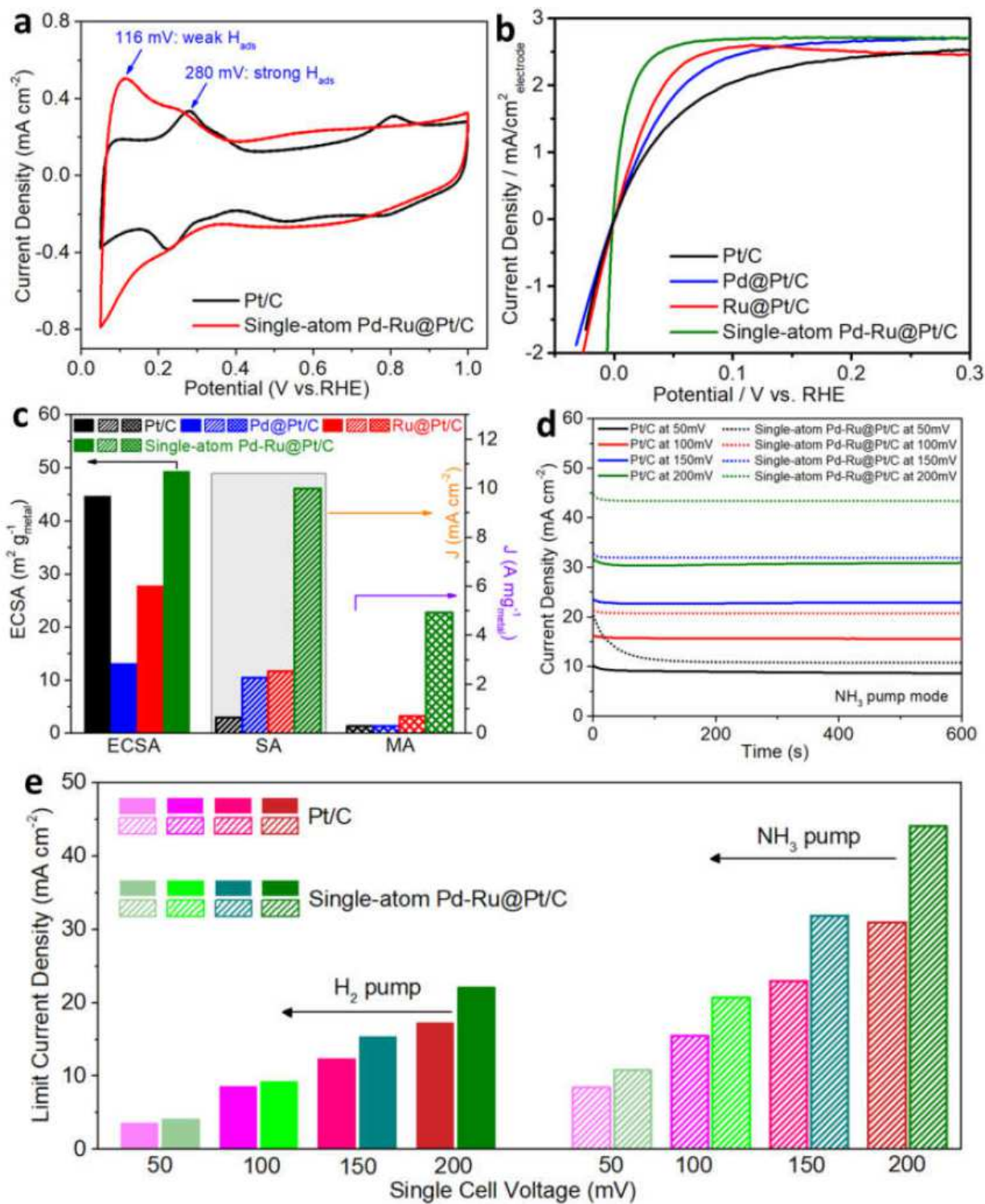


Figure 6

Electrochemical performance and mechanism of different catalysts. (a) CV curves of different catalysts. Test condition: 0.05 to 1.00 V vs. RHE, 50 mV/s, N₂-saturated 0.1M KOH. (b) HOR polarization curves of different catalysts. Test condition: -0.05 to 0.40V vs. RHE, 10 mV s⁻¹, H₂-saturated 0.1M KOH, RDE at 1600 rpm. (c) Comparison of ECSA (black arrow, left axis), SA (normalized by ECSA, orange arrow, right axis) and MA (normalized by Pt mass, purple arrow, right axis) for HER at 50 mV vs. RHE for all tested

catalysts. (d) Gibbs Free energy profiles for catalysts at equilibrium potential and pH = 14. (e) Comparison of limit current density of Pt/C and single-atom Pd-Ru@Pt/C under H₂ pump and NH₃ pump mode in electrochemical cell. Test condition: Nafion 211 membrane, 5 cm² electrode, 25 °C, 34% relative humidity (RH) for H₂-NH₃ mixture, 0.2 bar H₂-NH₃ mixture at flow rates of 50 mL min⁻¹ of H₂ and 100 mL min⁻¹ of NH₃.

Supplementary Files

This is a list of supplementary files associated with this preprint. Click to download.

- [Supportinginformation.pdf](#)